Identifying irrigated areas using land surface temperature and hydrological modelling: Application to Rhine basin

Devi Purnamasari[1,2], Adriaan J. Teuling[1], and Albrecht H. Weerts[1,2]

[1]Hydrology and Environmental Hydraulics Group, Wageningen University, the Netherlands
[2]Deltares, Delft, the Netherlands

Correspondence: Devi Purnamasari (devi.purnamasari@deltares.nl)

Abstract. Information about irrigation with relevant spatiotemporal resolution for understanding and modelling irrigation dynamics is important for improved water resources management. However, achieving a frequent and consistent characterization of areas where signals from rain-fed pixels overlap with irrigated pixels has been challenging. Here, we identify irrigated areas using a novel framework that combines hydrological modeling and satellite observations of land surface temperature. We tested
5 the proposed methodology on the Rhine basin covering the period from 2010 to 2019 at a 1 km resolution. The result includes multiyear irrigated maps and irrigation frequency. Temporal analysis reveals that an average of 159 thousand hectares received irrigation at least once during the study period. The proposed methodology can approximate irrigated areas with R^2 values of 0.79 and 0.77 for 2013 and 2016 compared to irrigation statistics, respectively. The method approximates irrigated areas in regions with large agricultural holdings better than in regions with small fragmented agricultural holdings, due to binary
10 classification and the choice of spatial resolution. The irrigated areas are mainly identified in the established areas indicated in the existing irrigation maps. A comparison with global datasets reveals different disparities due to spatial resolution, input data, reference period, and processing techniques. From multiyear analysis, it is evident that irrigation extent is positively correlated with precipitation (r = 0.73, p-value = 0.0163) and less with potential evapotranspiration.

1 Introduction

15 The expansion of irrigated areas, resulting from the concurrent effects of a growing population and climate change, is expected to continue to exert pressure on water resources (Döll and Siebert, 2002). In regions experiencing a warmer and drier climate, increase in crop evapotranspiration has resulted in increased net irrigation water to maintain or improve agricultural yields (Fader et al., 2016; Fischer et al., 2007). However, several studies show that the availability of water in the future will be negatively affected by changes in temperature and precipitation, raising concerns about whether there will be enough water
20 to meet the growing demand (Konapala et al., 2020; Boretti and Rosa, 2019). For example, interventions in water resource management in arid and semi-arid regions are necessary to address the growing demand for irrigation water, especially in the context of reduced water availability and increased temperature (Fader et al., 2016). As freshwater resources continue to decrease and demand for irrigation water continues to increase, it is becoming essential to develop models that monitor and manage irrigation water demands for water resources management.

25   Recent summer drought events in the early 21st century have been exceptional, characterized by widespread soil moisture deficits and a significant decrease in water resource availability (Spinoni et al., 2018; Hanel et al., 2018). These events have had a profound impact on the agricultural sector, for example, reported losses in agricultural yields in 2018 surpassing 50% compared to the average yield of the previous five years (Toreti et al., 2019). In the future, farmers may increasingly turn to irrigation to mitigate crop losses. However, this potential increase on agricultural water demand can create conflicts with

30   other water users. The Rhine basin serves as an example, being one of the major northern humid rivers affected by recent extreme droughts through its sensitivity to evapotranspiration (Buitink et al., 2021). It experienced extremely low water levels in consecutive summer months of 2018–2019 that caused water supply bottlenecks and disruptions in inland navigation in Germany (BfG, 2019). While past drought events have been studied in terms of their frequency and severity, there remains limited understanding of the vulnerability of water resource management and irrigation strategies during such events. It is

35   crucial to further explore irrigation management strategies in these regions to enhance our understanding of the challenges and risks posed by shifting climatic conditions and emerging water use conflicts (Toreti et al., 2019; Laaha et al., 2017).

    Identifying where irrigation occurs and how it evolves over time can offer improved insight into water use for sustainable water resources planning and management. Unfortunately, maps with irrigation extent with relevant spatial and temporal resolution for water management at the basin level are often lacking. This results in challenges in estimating irrigation water

40   requirements and developing hydrological models. Most research efforts have focused on monitoring the spatiotemporal extent of irrigated areas and quantifying irrigation rates in arid and semi-arid climates (see the Murray-Darling basin (Peña-Arancibia et al., 2016); the Ebro basin (Dari et al., 2021); the Miandoab plain in Iran (Jalilvand et al., 2019)). For the Rhine basin, the primary source of information on irrigated areas comes from sub-national statistics which are data sources for developing previous global maps of irrigated areas (GMIA (Siebert et al., 2005), MIRCA2000 (Portmann et al., 2010)). There is an increasing

45   need to expand these research efforts for better informed decisions in water resources management. In humid and temperate regions, shifting climatic conditions may offer advantages to the agricultural sector as larger areas become more suitable for crop cultivation which lead to a potential increase in irrigation water demands (Iglesias et al., 2012).

    In basin-wide water management, the use of earth observation products may be the only option to identify irrigated areas and irrigation events at relevant scales, especially considering the limitations of ground-based estimates due to cost inefficiency

50   and limited coverage. Researchers have extensively used remotely sensed vegetation indices, such as the Normalized Difference Vegetation Index (NDVI) or the Enhanced Vegetation Index (EVI), derived from optical sensors to detect irrigated areas in large regions (Ambika et al., 2016; Deines et al., 2019; Ozdogan and Gutman, 2008; Peña-Arancibia et al., 2016). These indices typically capture vegetation health and growth stages, with irrigated fields exhibiting higher values compared to adjacent non-irrigated fields. However, in temperate regions, distinguishing between irrigated and non-irrigated croplands using

55   vegetation indices in classification analysis presents challenges. These challenges arise because irrigation in these areas often supplements rainfall, potentially overlapping with the spectral signatures of non-irrigated pixels. Previous mapping studies suggest to include additional information such as climatic information, land use maps, and other remote sensing data sets to improve the identification of irrigated fields (Peña-Arancibia et al., 2016; Deines et al., 2019; Ozdogan and Gutman, 2008).

To address challenges associated with identifying irrigated areas, we propose a methodology that integrates surface energy to water balance in a hydrological model through evapotranspiration (ET). This methodology is based on the understanding that irrigation water use accounts for a significant portion of consumptive water loss in the form of actual evapotranspiration, which is governed by climatic conditions (Peña-Arancibia et al., 2016; Droogers et al., 2010). Existing approaches often involve comparing satellite-based retrievals with estimated ET fluxes derived from hydrological models. However, the accuracy of satellite-based evapotranspiration retrievals depends on how well the partitioning of evapotranspiration is modeled, which is still largely unvalidated (Talsma et al., 2018; Wang and Dickinson, 2012). In our study, we will add a surface energy balance module to link evapotranspiration estimates of a hydrological model to land surface temperature, allowing for direct comparison with satellite observations. Additionally, the key point of using land surface temperature data for mapping irrigated areas lies in its sensitivity to vegetation water stress. During water-limited conditions, reduced evapotranspiration increases the land surface temperature that drives an increase in sensible heat flux. In contrast, under irrigation, the land surface temperature of irrigated areas tends to be lower compared to adjacent non-irrigated croplands.

This paper investigates the potential of using evapotranspiration estimates from a spatially distributed hydrological model to detect and monitor irrigated areas at a resolution of approximately 1 km^2. Initially, we derive latent heat flux from the estimated evapotranspiration to solve surface energy balance terms. The spatial representativeness of the distributed hydrological model in providing evapotranspiration estimates is evaluated against another evapotranspiration product. Then, land surface temperature estimates are computed based on sensible heat flux and compared with observed land surface temperatures. To distinguish irrigated from non-irrigated areas, we use a supervised classification model trained and tested on a dataset collected from satellite observations with higher spatial resolution and apply the model to aggregated land surface temperature differences. Our research aims to address the following questions based on the outcomes of this study:

1. Could the difference in land surface temperature between simulated values from evapotranspiration estimates from the wflow_sbm model and satellite observations identify irrigated areas when compared against available regional statistics of irrigated areas or existing irrigated maps?

2. What is the extent of the irrigated areas in the Rhine, and what controls its interannual variability?

2 Data and methodology

2.1 Study area

We tested the proposed methodology to identify irrigated areas in the Rhine basin as shown in Figure 1. It drains an area of approximately 160,000 km^2. Figure 1b shows land uses and land cover in the basin, where agriculture occupies approximately 46% of total land use according to Copernicus CORINE land cover data (CLC 2018) (European Environment Agency, 2018). The agricultural fields are characterized by the cultivation of various crops, including cereals, oilseeds, potatoes, and sugar beets. A notable feature of this agricultural landscape is the prevalence of irrigation systems in the Middle Rhine catchment, which stretches from south to north along the border between France and Germany. Supplementary irrigation is commonly

Figure 1. Overview of the Rhine basin: **(a)** the sub-basins from HydroSHEDS (Lehner et al., 2008) and a digital elevation model (Farr et al., 2007), **(b)** aggregated land use and land cover from the CORINE Land Cover 2018 (European Environment Agency, 2018), **(c)** NUTS level 2 regions for which the reported total irrigated area was used to evaluate the results of classification analysis. The demarcated red line on panel **(a)** shows one of the croplands used to collect training and test data for building supervised classification model. Hashed regions indicate areas where irrigated area data are not available.

practiced during the summer months to prevent agricultural loss. Sources of irrigation come primarily from surface water bodies, groundwater bodies, reclaimed wastewater, and rainwater collection. Based on the EU Water Framework Directive (2000/60/EC) (WFD), each EU member state is required to regulate water abstraction through prior authorization regimes and provide incentives for efficient water use. For example, France has introduced taxation and mandatory metering as economic

95 instruments related to surface and groundwater abstraction (Berbel et al., 2019)

Precipitation and potential evapotranspiration play important roles in determining water availability and demand for irrigation. Table 1 summarizes the mean seasonal precipitation and potential evapotranspiration in the Rhine basin for 2010–2019. The Middle Rhine and East Alpine subbasins are representative of the two main seasonal cycles in the basin. The East Alpine region had higher precipitation than potential evapotranspiration compared to other subbasins, while the Middle Rhine had

100 relatively similar annual precipitation and evapotranspiration rates. However, the evapotranspiration rate in spring (MAM) and summer (JJA) often surpasses the precipitation, reflecting a potential for a water-limited regime. These fluctuations in precipitation and evapotranspiration throughout the year can influence the extent of irrigated areas annually. However, publicly

Table 1. The mean seasonal (DJF, MAM, JJA, and SON) precipitation and potential evapotranspiration of the Rhine sub-basins from 2010–2019.

Sub-basins	Precipitation [mm year^{-1}]				Potential Evapotranspiration [mm year^{-1}]			
	DJF	MAM	JJA	SON	DJF	MAM	JJA	SON
Middle Rhine	235	198	240	238	59	220	320	70
East Alpine	286	314	448	307	62	222	313	75

accessible data regarding multiyear irrigated maps of the Rhine basin are currently unavailable. The available information at the sub-national level (NUTS 2 unit) as shown in Figure 1c, compiled by Eurostat, primarily relies on summaries derived from the Farm Structure Surveys (FSS) conducted by EU member states. To identify irrigated areas within the Rhine basin, training and test data for supervised classification were collected from regions where irrigated plots can be identified through remote sensing observations, as described in Section 2.4.2.

2.2   Daily ET$_a$ from wflow_sbm

The wflow_sbm (van Verseveld et al., 2024) is a spatially distributed hydrological model designed to solve hydrological processes numerically at the grid cell. It accounts for several key hydrological processes: 1) canopy interception, 2) snow and glaciers, 3) soil moisture module and evapotranspiration, 4) lateral subsurface flow, 5) surface routing, and 6) reservoirs and lakes. The model takes both vertical and lateral processes into account when partitioning precipitation into storage, drainage, and evapotranspiration. Vertical processes are conceptualized as a soil bucket with saturated and unsaturated storage similar to Topog_SBM (Vertessy and Elsenbeer, 1999), while the lateral components (surface and subsurface flows) are routed using the kinematic-wave approximation. In this study, our focus lies on the evapotranspiration estimates of wflow_sbm due to its association with the land surface energy balance. The following gridded data sets, provided in daily temporal resolution and with a spatial resolution of 1 km, were used to compute water balance in wflow_sbm. The choice of a 1 km spatial resolution is deemed relevant and sufficient for conducting assessments at the river basin level.

1. The precipitation data are obtained from the HYRAS data set, which was developed by the German Meteorological Service (DWD) and the Federal Institute of Hydrology (BfG) (Rauthe et al., 2013).

2. The mean air temperature (Van Osnabrugge et al., 2019) was derived from interpolating ground measurements with topographic correction based on the lapse rate.

3. Potential evapotranspiration (Van Osnabrugge et al., 2019) was estimated based on the Makkink equation using ground observations of mean air temperature and downward shortwave radiation estimates from satellite products.

Evapotranspiration in wflow_sbm is expressed as a fraction of potential evapotranspiration that changes according to the amount of available water in the rooting zone (Feddes et al., 1976). Thus, the spatial variations of evapotranspiration across

different land uses inherently varies depending on the rooting depth of vegetation, which can be inferred from information provided by the soil map. The model represents the soil as a column with several layers, allowing it to account for vertical water movement and variations in soil moisture. The movement of water in the unsaturated soil layer follows the Brooks–Corey

130 model, which relates to the vertical saturated hydraulic conductivity and soil matrix potential. The rate of soil evaporation from unsaturated soil layers varies according to the fraction of vegetation roots and the soil moisture content that is related to the soil water holding capacity. Therefore, the representation of the soil water holding capacity is crucial for estimating soil moisture and consequently evapotranspiration in the wflow_sbm model.

Here, we use the most recent wflow_sbm schematization and parameterization as developed for the Dutch Ministry of

135 Infrastructure and Waterways (see the report by Buitink et al. (2023)). For more detailed information on the parameterization of the wflow_sbm model, calibration, and validation are provided in Imhoff et al. (2020) and Eilander et al. (2021). It is important to note that wflow_sbm does not incorporate land management practices, such as irrigation, which could potentially lead to an underestimation or overestimation of actual evapotranspiration. In this study, we conducted a brief evaluation of the spatial distribution of actual evapotranspiration estimated using the model parameters derived from PTFs by comparing it

140 against GLEAM version 3.8a (GLEAM) (Martens et al., 2017) for the period 2010–2019. In this analysis, we resampled the actual evapotranspiration observations from GLEAM to a finer resolution, preserving details at the 1 km spatial resolution of wflow_sbm.

2.3 Land surface temperature module

The aim of this study is to determine the spatiotemporal pattern of irrigated areas by using the land surface temperature

145 difference (ΔT_s). This difference is obtained by comparing the land surface temperature derived from evapotranspiration (ET_a) estimates obtained from the wflow_sbm model ($T_{s,sim}$) with those obtained from satellite observations ($T_{s,obs}$). To achieve this, we have developed a module that connects the partitioning of surface energy balance fluxes with evapotranspiration estimates. This additional module is based on a parsimonious model previously coupled with the mesoscale Hydrologic Model (mHM) developed by Zink et al. (2018). The energy balance of the land surface is calculated as follows:

150 $$R_n = LE + H + G \tag{1}$$

The land surface temperature is derived from the sensible heat flux, where it is obtained by resolving the energy balance at daily temporal resolution. As the magnitudes of the daytime soil heat flux G is relatively small compared to R_n, therefore the energy balance equation is expressed as follows:

$$H \approx R_n - LE \tag{2}$$

155 The evapotranspiration (mm day^{-1}), which is the water balance term provided by the wflow_sbm, is converted to latent heat flux LE in the following:

$$LE = \lambda \times \rho_{water} \times ET \tag{3}$$
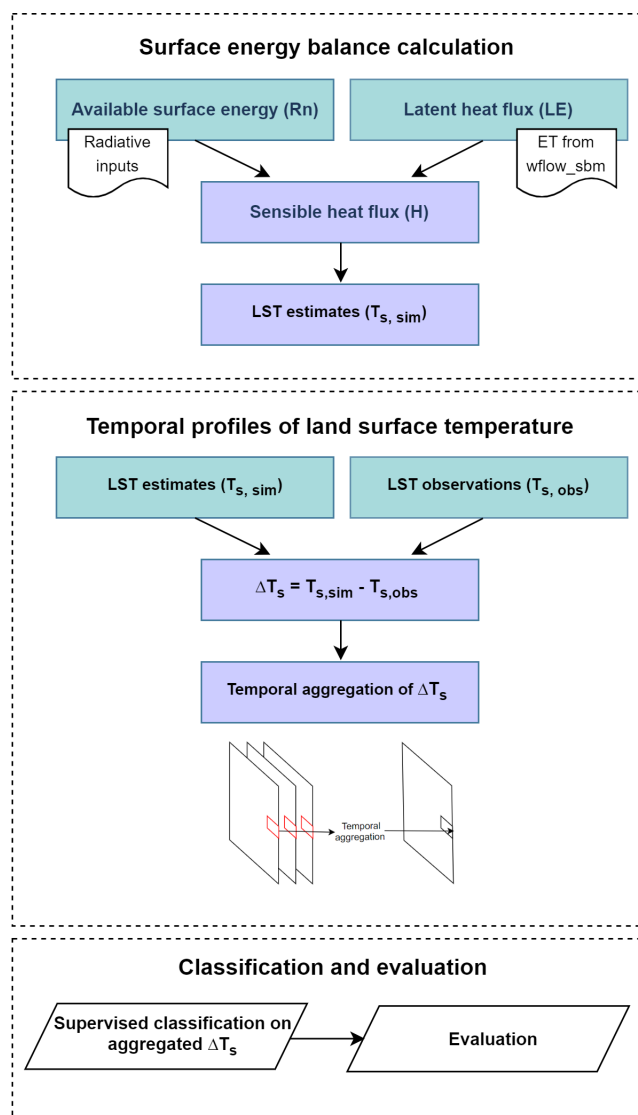
Figure 2. The workflow outlines the methodology for linking evapotranspiration estimates to derive land surface temperature. The spatiotemporal features of land surface temperature difference are used as input data to identify irrigated areas.

with ρ_{water} is 1,000 $kg\,m^{-3}$ and the latent heat vaporization λ equals:

$$\lambda = (2501 - 2.375T_a) \tag{4}$$

the evapotranspiration ET (mm day^{-1}) is estimated by wflow_sbm. Meanwhile, the net radiation R_n is calculated from radiation components from satellite observations which is calculated as:

$$R_n = R_s^{in} - R_s^{out} + R_l^{in} + R_s^{in} \tag{5}$$

$$R_n = R_s^n + R_l^n \tag{6}$$

The amount of outgoing shortwave radiation R_s^{out} that is reflected to space is determined by the surface albedo α. Therefore, to account the energy loss from the outgoing shortwave radiation, the net shortwave radiation R_s^n is calculated as using the following formula:

$$R_s^n = (1 - \alpha)R_s^{in} \tag{7}$$

The rate of energy loss from the outgoing long-wave radiation R_l^{out} is determined by the Stefan–Boltzmann law, where the Stefan–Boltzmann constant $\sigma = 5.67 \times 10^{-8} W m^{-2} K^{-4}$. The estimates of net longwave radiation are then calculated by adjusting the outgoing long-wave radiation based on humidity and cloudiness, as these factors impact the absorption and reflection of radiation fluxes (Allen et al., 1998).

$$R_l^n = (\sigma T_a^4)(0.34 - 0.14\sqrt{ea})\left(1.35\frac{R_s^{in}}{R_{so}} - 0.35\right) \tag{8}$$

$$e_a = 0.611 exp\left(\frac{17.27 T_a}{(T_a + 273.3)^2}\right) \tag{9}$$

The expression $(0.34 - 0.14\sqrt{ea})$ represents the impact of humidity on the net outgoing long-wave radiation. The term $1.35\frac{R_s^{in}}{R_{so}}$ expresses the impact of cloudiness on incoming shortwave radiation where R_{so} can be calculated as follows:

$$R_{so} = 0.75 R_a \tag{10}$$

$$R_a = G_{sc} d_r (\omega_s \sin\phi \sin\delta + \cos\phi \cos\delta \sin\omega_s) \tag{11}$$

where the magnitude of extraterrestrial radiation R_a are determined based on solar constant, inverse relative distance Earth–Sun d_r, sunset hour angle ω_s, latitude ϕ, and solar declination δ. Therefore, the sensible heat flux equation becomes:

$$H = (1 - \alpha)R_s^{in} + (\sigma T_a^4)(0.34 - 0.14\sqrt{ea})\left(1.35\frac{R_s^{in}}{R_{so}} - 0.35\right) - LE \tag{12}$$

Then, the land surface temperature T_s can be computed as follows:

$$T_s = \frac{H r_a}{\rho_a c_p} + T_a \tag{13}$$

In summary, the land surface temperature T_s is calculated using the following inputs: R_s^{in} and α obtained from satellite observations, T_a represents the mean air temperature and serves as an input for the wflow_sbm model, LE derived from the evapotranspiration calculated by the wflow_sbm, and r_a represents the aerodynamic resistance.

The aerodynamic resistance r_a that governs the vapour and heat transfer is computed based on Thom's equation 1975 and roughness parameters recommended by Allen et al. (1998):

$$r_a = \frac{\ln\left(\frac{z_m - d}{z_{om}}\right) \ln\left(\frac{z_h - d}{z_{oh}}\right)}{k^2 u_z} \tag{14}$$

$$d = \frac{2}{3} h_c \tag{15}$$

190

$$z_{om} = 0.123 h_c \tag{16}$$

$$z_{oh} = 0.1 z_{om} \tag{17}$$

where d is the zero plane displacement height, z_m is the height of wind measurement, z_h is the height of humidity measurement, z_{oh} is the roughness length of vapour and heat transfer, z_{om} is the roughness length of momentum transfer, u_z is the wind speed measured at the height of 2 m, h_c is the crop height, and von Karman constant $k = 0.41$. In this study, the height of measurements

195   for wind and humidity are assumed to be equal ($z = z_m = z_h$). During periods of extremely low wind conditions, the wind speed is constrained to be greater than 0.5 m s^{-1} to consider vapor exchange on the surface induced by air buoyancy and layer instability effects (Allen et al., 1998).

The proposed land surface temperature module requires additional radiative terms as input. For this study, data from the geostationary satellites Meteosat Second Generation (MSG): the downward shortwave radiation (LSA-SAF DSSF) and surface

200   albedo (LSA-SAF AL) at a spatial resolution of 3 km (Trigo et al., 2011) were used as radiative input data. As there is limited availability of daily land surface albedo data since 2009, we use 10-daily land surface albedo which available from 2005 onwards.

2.4 Identifying irrigated area

2.4.1 Classification method

205   Irrigated areas in the Rhine basin were identified with a combination of hydrological model of wflow_sbm and satellite observations of land surface temperature as shown in Figure 3. As illustrated in Figure 3a, wflow_sbm does not physically represent irrigation practices. Meanwhile, satellite observations capture irrigation signals as an additional source of evapotranspiration in the water balance that modulates the partitioning of surface energy (Figure 3b). This translates to higher latent heat flux and lower sensible heat flux than what the hydrological model predicts. Higher partitioning of available surface energy for latent

210   heat flux results in lower land surface temperature. Consequently, simulated land surface temperature data that were derived from evapotranspiration estimate ($T_{s,sim}$) as described in Section 2.3 will be higher than observed land surface temperature ($T_{s,obs}$). However, on a surface where there is no additional source of evapotranspiration, there are no changes in the energy and water balance fluxes. Figure 3d and 3e show the time series of $T_{s,sim}$, $T_{s,obs}$, and ΔT_s, where an irrigated pixel in a hydrological model exhibits a higher magnitude of ΔT_s than a neighboring non-irrigated cropland pixel, which remains relatively

215   constant throughout the year. To classify irrigated area, the following data were used to compute ΔT_s and listed below:
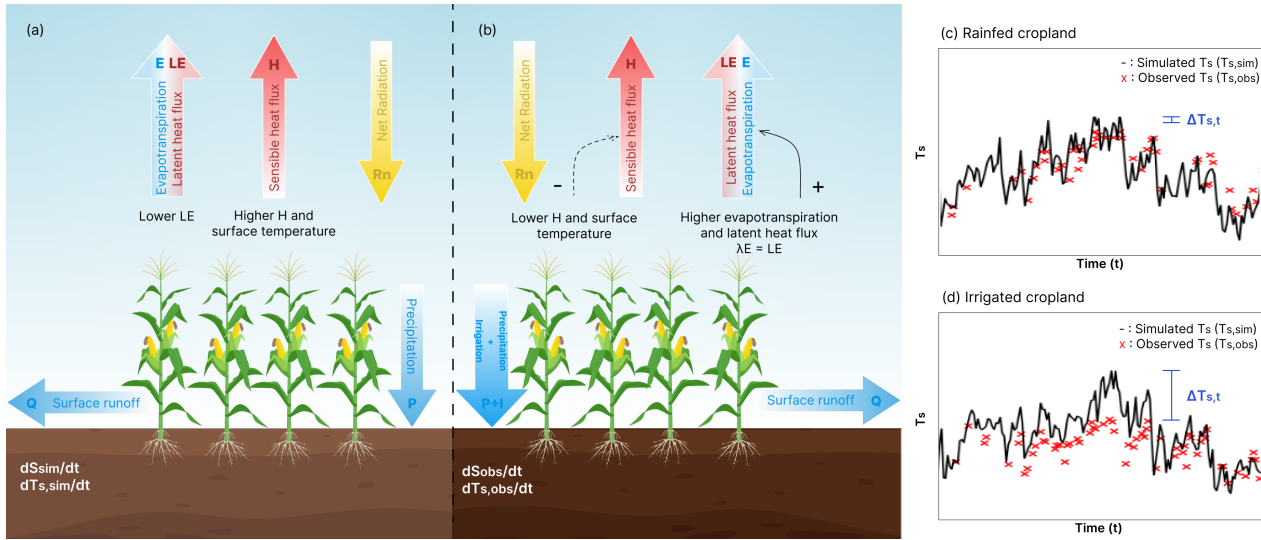
Figure 3. Schematic of the energy and water balance in **(a)** hydrological model wflow_sbm that does not represent irrigation practices, and **(b)** earth observations that capture irrigation signals. In this study, we use land surface temperature observations. $T_{s,sim}$ refers to land surface temperature that is derived from sensible heat flux after relating evapotranspiration in water balance to latent heat flux in energy balance through λ. Irrigation increases the partitioning of available energy to latent heat flux, leading to lower $T_{s,sim}$. **(a)** The magnitude of $T_{s,obs}$ of the non-irrigated croplands is slightly similar to $T_{s,sim}$ where **(b)** $T_{s,obs}$ is lower than $T_{s,sim}$ due to higher evapotranspiration.

1. Land surface temperature at 1 km resolution as $T_{s,obs}$ from MODIS sensor aboard Terra and Aqua (Wan et al., 2021a, b). MODIS observation data were resampled and reprojected from sinusoidal to the geographic coordinate system.

2. Simulated actual evapotranspiration from wflow_sbm. These estimates were used to derive corresponding $T_{s,sim}$ from the available surface energy balance.

In this study, irrigated areas are defined as pixels where irrigation is detected within a given year. In cases where irrigation events are recurrent within the same year, these events are counted as a single event. Due to data gaps resulting from cloud cover and sampling frequency limitations in observations, cloud-free and gap-free daily ΔT_s data were aggregated over one year. To capture spatiotemporal features, we used statistical measures: p_{10}, p_{50}, p_{90}, mean, and standard deviation to aggregate equidistant observations into an annual data cube. The use of spatiotemporal features has been a common practice in previous irrigation mapping studies. For example, Dari et al. (2021) used the spatiotemporal dynamics of soil moisture, including day-to-day variability, as a feature in k-means clustering to distinguish between irrigated and non-irrigated land in the Mediterranean. After computing ΔT_s, we applied the random forest algorithm by Breiman (2001) to classify irrigated and non-irrigated pixels. The results were screened to remove pixels that were identified as irrigated only once during the study period as the installation cost of irrigation equipment is high. The resulting estimation distinguishes between irrigated and non-irrigated pixels and does not produce irrigation fraction of the entire pixel area.
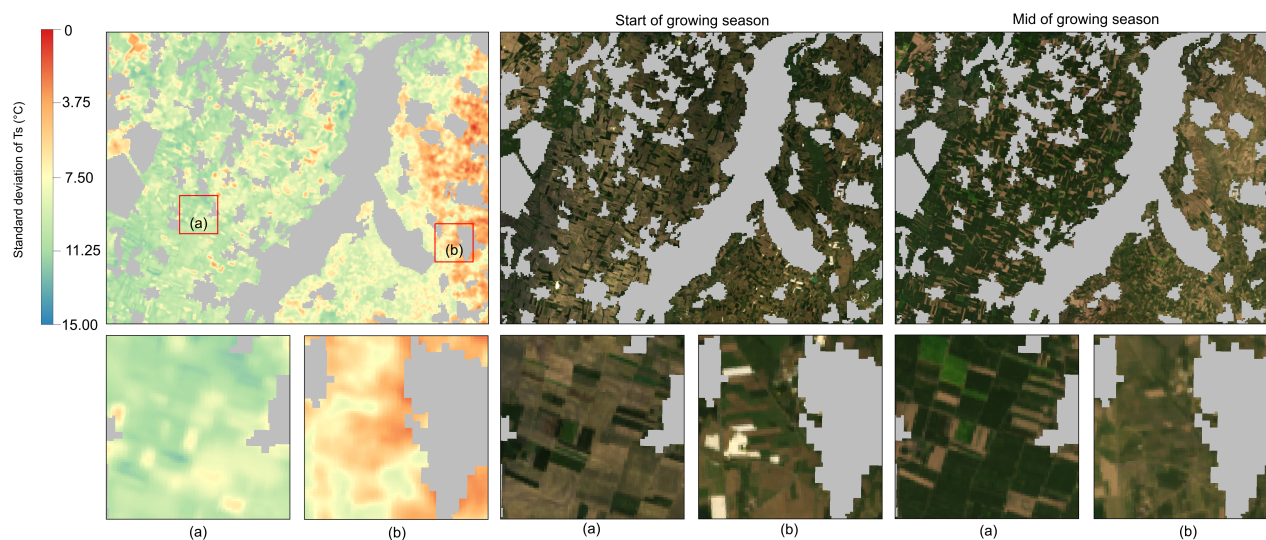
Figure 4. Illustration for training and test dataset: a snapshot of cropland area within the basin (the location is marked by a red rectangle in Figure 1a) showing the seasonal standard deviation of land surface temperature (T_s) alongside true-color images collected from Landsat annual cloud-free composite images (April–September). It reveals that irrigated areas in panel **(a)** exhibit a lower standard deviation in land surface temperature, whereas non-irrigated areas in panel **(b)** show a higher standard deviation. Gray shaded areas are masks for noncropland land cover.

2.4.2 Training and test dataset for random forest classification

Dataset for building random forest classification were acquired inclusively for each year for the period 2010–2019 to account for possible variations in the irrigated area due to climate conditions. Those dataset were collected from high-resolution imagery from Landsat 7 and 8 with a spatial resolution of 30 meters (visible) and 100 meters (thermal) as shown in Figure 4. The training method used in this step draws on heuristic techniques used in previous remote sensing studies (Peña-Arancibia et al., 2016; Deines et al., 2019; Shahriar Pervez et al., 2014), as elaborated below:

1. Data were generated using high-resolution true-color images captured during the growing season. These images were particularly valuable in identifying irrigated fields at the beginning of the growing season. During this specific period, visual identification of plots under irrigation or equipped with irrigation was feasible.

2. True-color images were plotted concurrently with thermal observations to distinguish irrigated pixels from neighboring pixels. Additionally, this prevents misinterpretation of pixels with darker soil resulting from ploughing as irrigated pixels. When such conditions are observed, these pixels are labeled as "non-irrigated." All training labels follow a binary classification that distinguishes between irrigated and non-irrigated pixels.

The time series of ΔT_s was also used to explore the potential presence of irrigated pixels. When potential irrigated pixels from Landsat true-color and thermal images were identified, a noticeable increase in ΔT_s was observed. In cases where these

temperature differences did not correspond to agricultural land parcels identified from land cover map, it was inferred that these variations might arise from alternative sources or could be influenced by the presence of neighbouring land cover types, such as floodplain and forests. Consequently, the pixels were labelled as "non-irrigated". The dataset obtained from high-resolution imagery was divided into two subsets: 80% for a training set and 20% for a test set. The test set was used to assess the

250 performance of the model, which was trained using the training data. Detailed information on the metrics used to evaluate the model and its performance is summarized in the Appendix A.

2.4.3 Evaluation data

The implementation of a classification analysis using a random forest classifier has produced a series of 10 annual irrigation maps from 2010 to 2019. The validation of these maps involves both temporal and spatial assessments of the irrigated areas.

255 Unfortunately, there are no datasets available for this purpose. Given the absence of ground-based observational data on irrigated areas, our multiyear classification assessment relies on comparisons with irrigation statistics. Specifically, national-level statistics regarding irrigated areas within the basin were obtained from the statistical office of the European Union, Eurostat, for the years 2013 and 2016 at the NUTS 2 (indicator: ef_poirrig). These statistics were sourced from the FSS, where differences in methodologies and variables between countries could cause potential uncertainties in the report. The data area available

260 at https://ec.europa.eu/eurostat/data/database. Additionally, data on irrigated areas in Germany for 2019 were provided by the Federal Statistics Office of Germany. The comparison between the mapped area and reported area for each NUTS 2 regions were mapped to evaluate differences between data sets.

To further asses the consistency and accuracy of irrigated areas, the spatial distribution of the irrigated area was compared to the existing irrigated maps: Global Irrigated Area Map (GIAM) (Thenkabail et al., 2009), Global Map of Irrigated Areas

265 (GMIA) (Siebert et al., 2013), MIRCA2000 (Portmann et al., 2010)), and Global Irrigated Area (Meier et al., 2018) as summarized in Table 2. The first three products were developed at a 5 arc-minute resolution, while the latter was developed at a 1 km spatial resolution. MIRCA2000 and GMIA used sub-national statistics and geographical information on the location of irrigation schemes as references to produce maps detailing irrigation portion. Meanwhile, GIAM and Global Irrigated Area made use of remote sensing products and techniques to provide irrigation maps in binary format. Specifically for the Global

270 Irrigated Area, it used NDVI to downscale the distribution of irrigation indicated in GMIA.

3 Results

3.1 Spatial distribution of ET_a

Figure 5 shows comparison of mean annual actual evapotranspiration estimated from GLEAM (Figure 5a) and wflow_sbm (Figure 5b) which are summarized for various land cover classes (Figure 5c). As illustrated in Figure 5b, wflow_sbm solves the

275 water balance at a higher spatial resolution than GLEAM, enabling a more detailed representation of actual evapotranspiration across various land classes. Estimates of actual evapotranspiration for cropland, pasture, and sparsely vegetated classes exhibit

Table 2. Existing irrigation datasets to evaluate estimated irrigation extent of the Rhine basin.

Products	Resolution	Period	Coverage	Methods	Source
Global Irrigated Area Map (GIAM)	5 arc min	A single map, 2000	Global	Spectral matching techniques of remote sensing products	Thenkabail et al. (2009)
Global Map of Irrigated Areas (GMIA) v5.0	5 arc min	Single map, representative for the period 2000–2008	Global	Sub-national agricultural statistics and geographical information	Siebert et al. (2013)
MIRCA2000	5 arc min	Single map, representative for the period 1998–2002	Global	Sub-national agricultural statistics, harvested area, GMIA, and ancillary data	Portmann et al. (2010)
Global Irrigated Area	1 km	Single map, representative for the period 1999–2012	Global	Decision tree, NDVI, agricultural suitability, GMIA	Meier et al. (2018)
Eurostat statistics	Regional statistics of area irrigated at least once a year at NUTS 2	3-year interval (2013, 2016)	European Union	Farm Structure Survey (FSS)	https://ec.europa.eu/eurostat/data/database

lower medians in wflow_sbm compared to GLEAM. Meanwhile, the overall spatial distribution of actual evapotranspiration for forests closely resembles GLEAM estimates. It is important to highlight that wflow_sbm estimates lower actual evapotranspiration for urban areas compared to GLEAM, primarily because GLEAM does not incorporate urban characteristics into its
280 model. To ensure consistency, other land use classes except for agricultural land were masked out from the classification task to minimize misclassification due to additional evapotranspiration sources in non-agricultural land. This comparison primarily serves to provide information on the spatial distribution of evapotranspiration rather than for validation purposes as GLEAM functions as a land surface model that assimilates microwave surface soil moisture observations from the ESA Climate Change Initiative soil moisture (ESA CCI SM) (Wagner et al., 2012; Liu et al., 2012) and the Soil Moisture and Ocean Salinity (SMOS)
285 soil moisture product (Jacquette et al., 2010) to improve estimation of evaporation components.

3.2 Land surface temperature from hydrological modelling

Figure 6 shows an example temporal profiles of average basin precipitation and evapotranspiration and land surface temperature for both irrigated (Figure 6b) and non-irrigated pixels (Figure 6c) for training data. Despite high precipitation from January
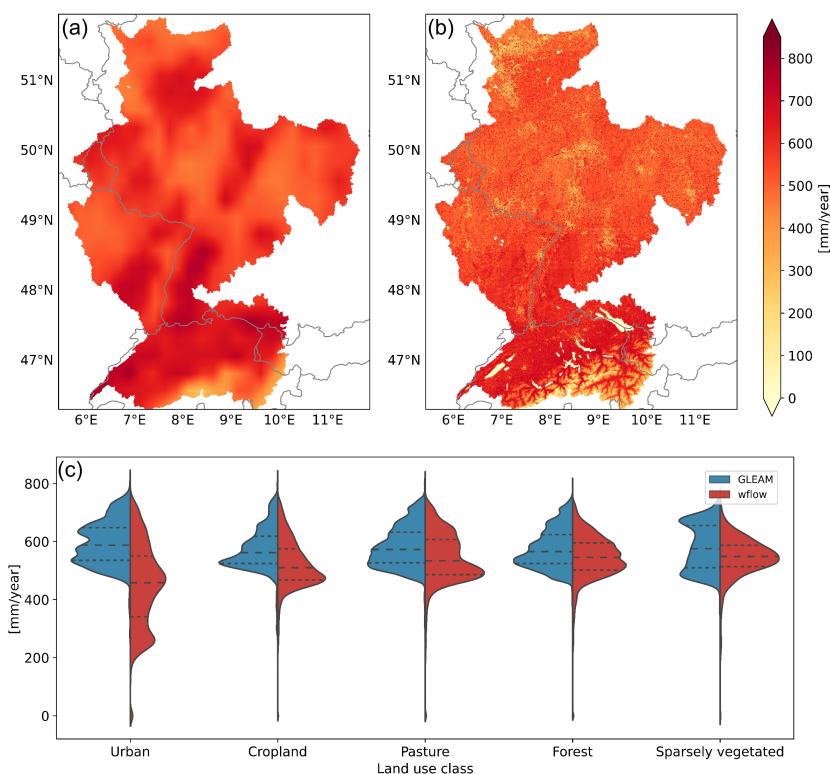
Figure 5. Mean annual actual evapotranspiration of **(a)** GLEAM version 3.8a and **(a)** wflow_sbm from 2010–2019. The kernel density plot on panel **(c)** summarizes the annual rate of evapotranspiration in urban, cropland, pasture, forest, and sparsely vegetated areas. The dashed lines represent the third, median, and first quartile.

to the end of April, the low potential evapotranspiration during this period does not contribute to an additional source of latent

290 heat flux due to limited available surface energy. As a result, $T_{s,sim}$ for both irrigated and non-irrigated pixels closely resemble $T_{s,obs}$. However, differences between $T_{s,sim}$ and $T_{s,obs}$ become more apparent in irrigated pixels as potential evapotranspiration gradually increases from the beginning to the peak of the growing season, reaching differences of up to approximately 10°C. Following the peak, ΔT_s gradually declines towards the end of the growing season corresponding to the potential evapotranspiration rate with a lag. In contrast, ΔT_s of non-irrigated pixels remains relatively constant during the growing season

295 despite the gradual increase in potential evapotranspiration. As ΔT_s gradually increases towards the peak of growing seasons on irrigated pixels, it leads to higher annual ΔT_s variability compared to non-irrigated pixels. These observed ΔT_s across irrigated pixels suggest the presence of other sources of evapotranspiration which were not considered in the model.

These the distinct daily temporal patterns of ΔT_s between irrigated and non-irrigated pixels were used to estimate annual irrigation extent. Figure 7 shows an example of statistical summaries of ΔT_s for irrigated and non-irrigated pixels in 2018 and

300 2019. Except for p_{10}, irrigated pixels show higher p_{50}, p_{90}, mean, and standard deviation relative to non-irrigated land due to
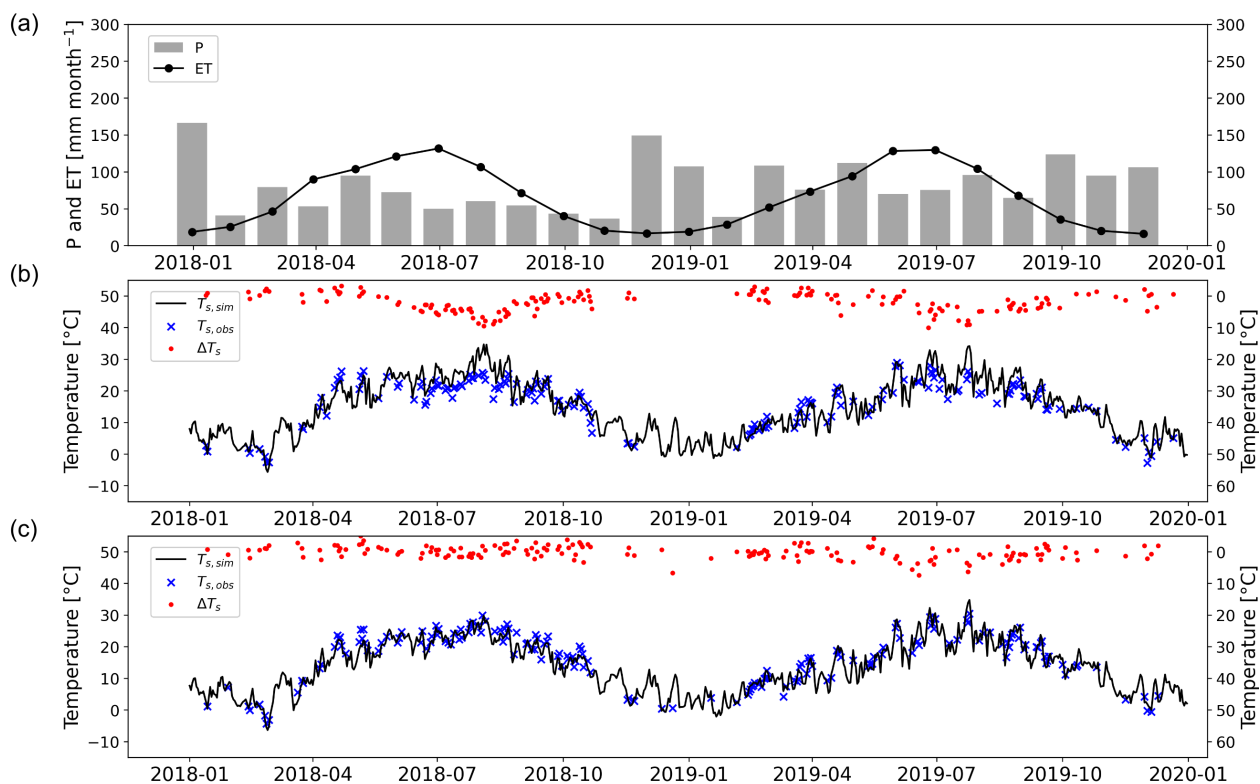
Figure 6. (a) Time series of monthly precipitation and potential evapotranspiration averaged across the basin alongside time series of simulated land surface temperature ($T_{s,sim}$) and observed land surface temperature from MODIS ($T_{s,obs}$). These are provided for pixels considered as **(b)** irrigated and **(c)** non-irrigated.

different temporal profile of ΔT_s. However, the magnitude of ΔT_s is more pronounced in dry years than in wet years, resulting in varying magnitudes in statistical summaries throughout different year. Consequently, a model trained with data from a specific year cannot be used identify irrigated areas for the whole study period due to varying meteorological conditions. This limitation affects the use of threshold-based methods and models trained on specific years, as they are prone to misclassification. Nonetheless, these distinct patterns in land surface temperature dynamics provide a basis for distinguishing irrigated from non-irrigated pixels.

3.3 Interannual variability of irrigated area

Figure 8 shows the comparison between the reported irrigated areas from Eurostat data and the mapped irrigated areas for years 2013 (Figure 8a) and 2016 (Figure 8b). As the linear fit is strongly influenced by regions with large irrigated areas, the datasets were transformed using a logarithmic transformation to assess the difference between the estimated and reported values in regions with limited irrigated areas. Overall, the mapped irrigated areas at NUTS level 2 show a good agreement

305

310
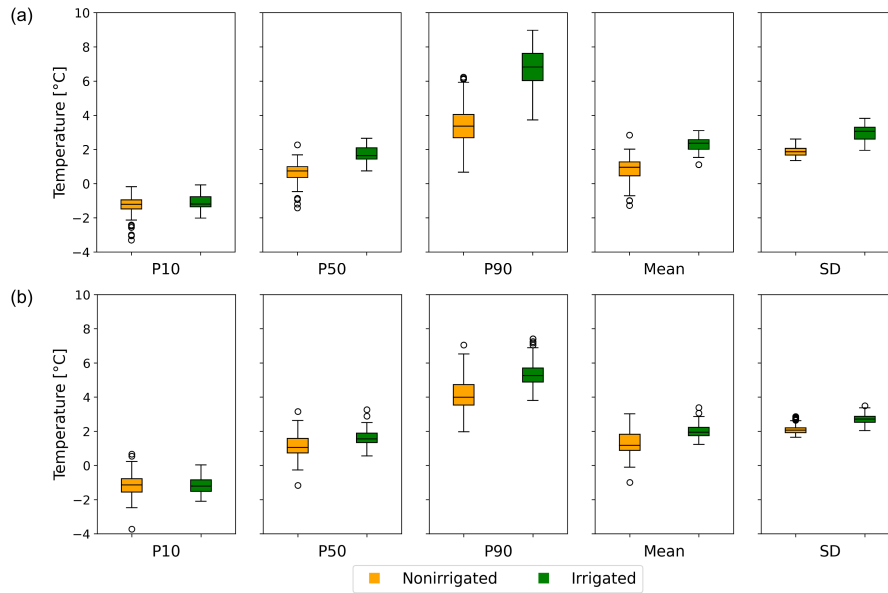
Figure 7. The box-plot shows statistical summary of training data for non-irrigated and irrigated pixels for **(a)** 2018 and **(b)** 2019.
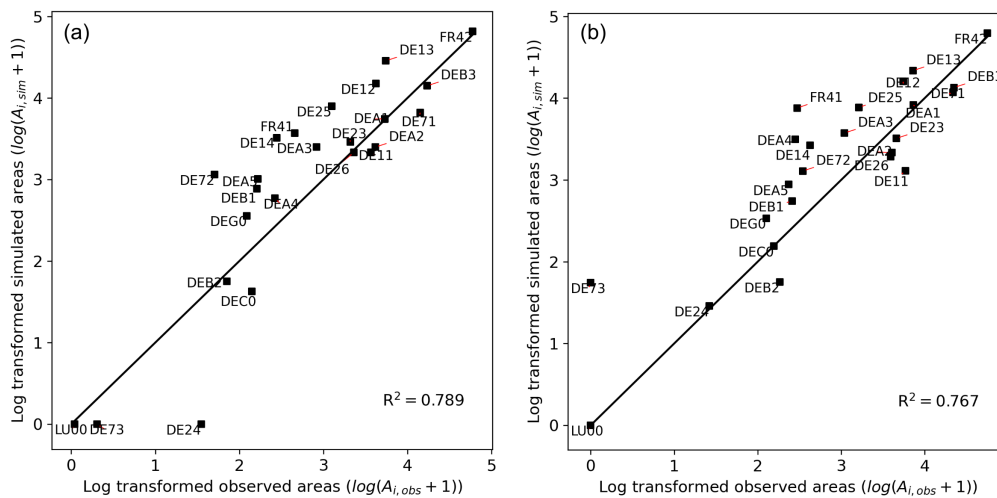
Figure 8. The mapped irrigated area of the Rhine basin as identified through classification ($A_{i,sim}$) is compared with the total irrigated areas reported in Eurostat data at NUTS level 2 ($A_{i,obs}$) for the years **(a)** 2013 and **(b)** 2016. The values of the total irrigated areas [× 1000 ha] were transformed using $\log(A+1)$ transformation.

with the reported irrigated areas, with R^2 values of 0.79 and 0.77 for 2013 and 2016, respectively. However, in some NUTS level 2 regions for both years, the mapped irrigated areas exceed the reported irrigated area, with an average percentage relative difference of 17% (ranging from 12% to 22%). This overestimation is particularly notable in regions characterized

315   by small-scale irrigation holdings where irrigation is sparsely distributed alongside mixed land use, such as Koblenz (DEB1), Mittelfranken (DE25), Tübingen (DE14), and Arnsberg (DEA5). Based on statistics reported by the Federal Statistical Office of Germany, these regions have an average irrigated area of 5–9 hectares per agricultural holding in 2019. The mapping methodology performed better in regions characterized by large irrigation holdings (with an average >22 hectares per holding), such as Alsace (FR42), Rheinhessen-Pfalz (DEB3), Düsseldorf (DEA1), Darmstadt (DE71), and Köln (DEA2).

320   The difference between our estimates and the irrigated area reported by official statistics can be attributed to two main factors: (i) the spatial resolution difference, and (ii) uncertainties in the reported irrigated areas. In our classification process, we do not adjust the area of a pixel identified as either irrigated or non-irrigated based on the size of agricultural holdings in the region, which may lead to overestimation in regions where agricultural holdings smaller than 1 km^2 are dominant. Meanwhile, the reported irrigated areas from Eurostat were collected through questionnaires distributed to several agricultural holdings.

325   Comparing continuous spatial information from classification results with point information obtained from questionnaires is not ideal. The scaling issues between these two types of data make direct comparison difficult and can lead to misinterpretation of the extent of irrigation in the region. To address this issue, the spatial distribution of irrigated areas was evaluated against current irrigation maps (see Section 3.4). Additionally, validating our maps poses challenges because of potential errors in the data collected from the FSS of 2013 and 2016. These surveys are subject to both sampling and non-sampling errors. The FSS

330   data collection involves random sampling methods and extrapolation techniques, potentially resulting in deviations between the randomized sampling result and the true value of the entire population (Eurostat, 2016).

       The same mapping methodology was applied to identify irrigated areas, providing details on the extent of irrigation in the Rhine basin from 2010 to 2019. Based on the average from ten annual maps, the irrigated area in the Rhine basin was estimated to be 159 thousand hectares, with the spatial distribution covering an area of 370 thousand hectares, as shown in Figure 9. The

335   irrigated areas were concentrated near Düsseldorf (DEA1), Köln (DEA2), Münster (DEA3) in the Lower Rhine (Figure 9b), Darmstadt (DE71) and Rheinhessen-Pfalz (DEB3) in the Main (Figure 9c), and Alsace (FR42) in the Middle Rhine (Figure 9d). Analysis of multiyear irrigated maps revealed that approximately 10 thousand hectares were consistently identified as receiving irrigation and were mostly found in Alsace. The mapped irrigated area at 1 km resolution allows for the observation of additional information that is difficult to identify in irrigated products with coarser spatial resolution. For instance, in the

340   Rhine valley, the spatial distribution of irrigated areas is predominantly concentrated to the east of the French–Germany border in the Alsace region, with higher density compared to neighboring agricultural lands in Freiburg.

       The spatial and temporal distribution of irrigated areas is influenced by irrigation management practices, which are partially driven by climatic factors such as precipitation and evapotranspiration. Figure 10 shows the correlations between precipitation, evapotranspiration, and their difference with yearly total irrigated areas. The analysis reveals a reduction in total irrigated area

345   during years with low precipitation (r = 0.73, p-value = 0.0163). In 2011, 2015, and 2018, the Rhine basin experienced lower annual precipitation coupled with higher evapotranspiration compared to the previous year. During these years, the annual average total irrigated area in the basin dwindled to 138 thousand hectares, 18.8% lower relative to the annual average of the remaining years. Figure 11 shows an example of the difference in irrigated area between 2018 and 2019, where the irrigated area in 2018 were lower than in 2019. This indicates that farmers likely irrigated a smaller area to cope with reduced water
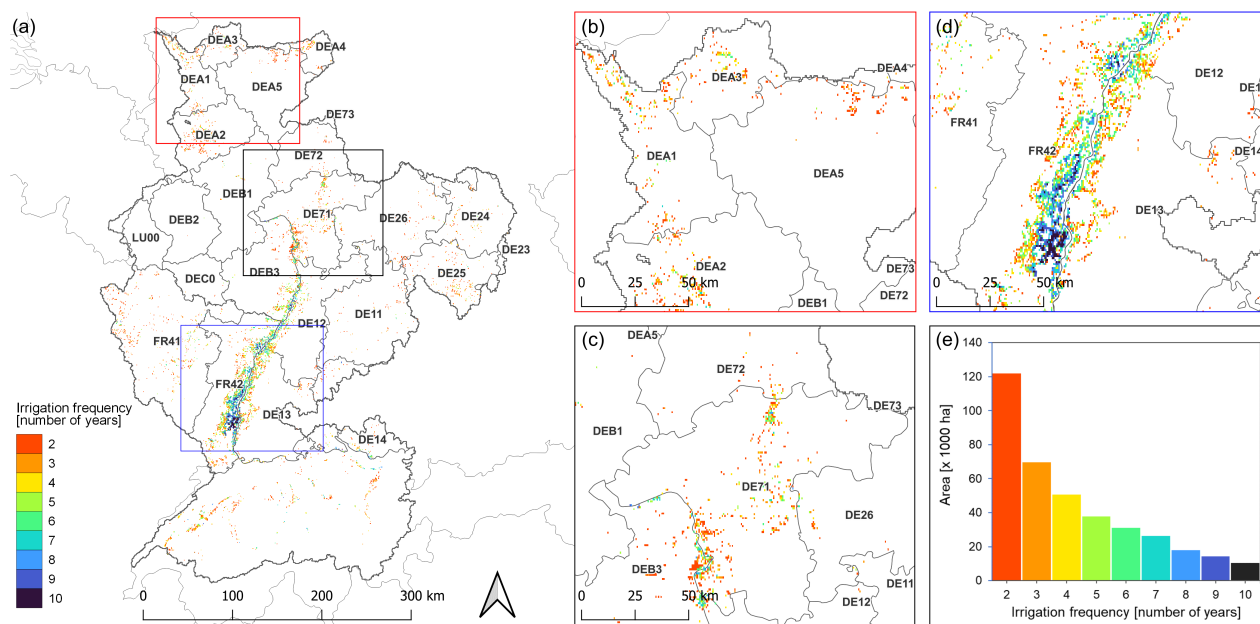
Figure 9. The extent of irrigated area derived from land surface temperature difference and irrigation frequency from the period 2010–2019. The rectangles on panel **(a)** show irrigation hotspots in: **(b)** the Lower Rhine, **(c)** the Middle Rhine, and **(d)** the Rhine valley. Panel **(e)** shows irrigation frequency and corresponding area.

availability. However, without access to irrigation volume datasets complementing information on irrigated areas, we cannot establish the relationship between irrigated area and water use. The observed variability underscores the necessity of collecting multiyear data on irrigated areas to enhance our understanding and management of water resources in agricultural regions. This pattern varies at the regional level, for instance, irrigated areas during dry years increased by 9% (6 thousand hectares) compared to the annual average during wet years in Alsace ($r = -0.82$, p-value = 0.004) as detailed in Appendix B.

3.4 Intercomparison with existing irrigated maps

The identified irrigated areas are mainly found in the already known irrigation scheme in the current maps with additional identified irrigated areas as shown in Figure 12. Potential discrepancies between existing products used in this study would be expected because of underlying differences in spatial resolution, input data, reference period, and processing techniques to derive irrigated areas. Our estimated irrigated area exceeds the actual irrigated area (AEI) reported by GMIA (148 thousand hectares) (Meier et al., 2018) and MIRCA2000 (110 thousand hectares) (Portmann et al., 2010). MIRCA2000 not only provides lower estimates for irrigated areas compared to GMIA, but also fails to accurately identify irrigated areas within the Main catchment and some part of the Lower Rhine catchment which were also reported in sub-national statistics from Eurostat. Although both use sub-national statistics as a reference, MIRCA2000 determines irrigated areas based on maximum monthly irrigated area that was estimated based on crop-specific harvested area from Monfreda et al. (2008) as input data. Thus, a
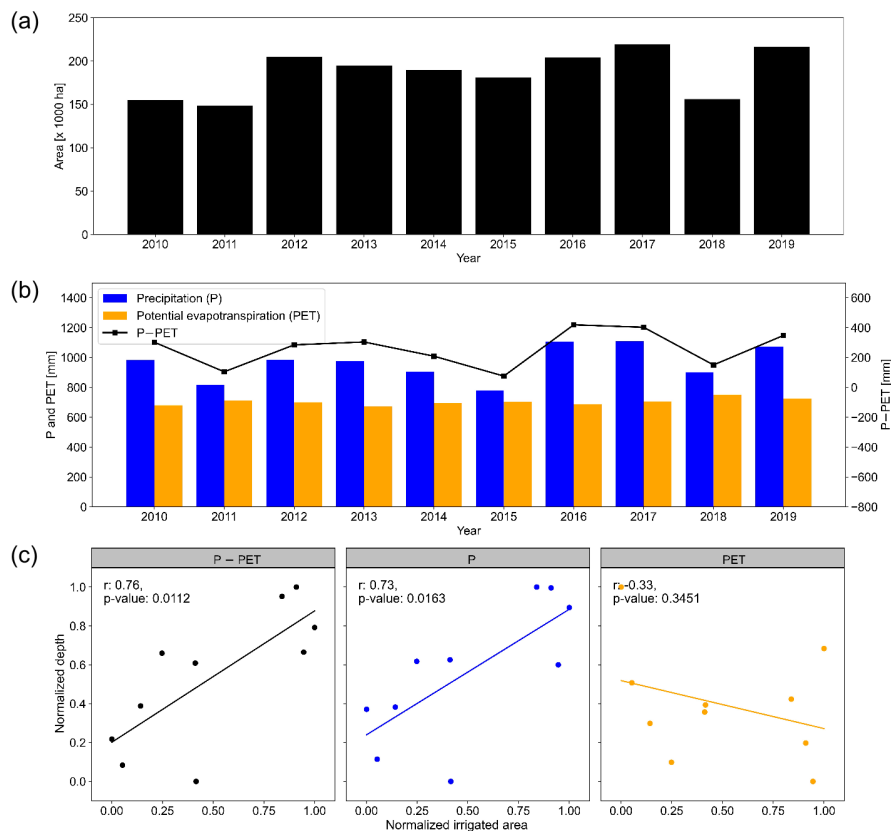
Figure 10. (a) The annual sum of climatic variables: precipitation, evapotranspiration, and the difference for the period from 2010 to 2019. **(b)** Linear regression analysis is performed for each climatic variable compared to the annual irrigated area.

significant harvested area that was not reported in the crop-specific harvested area data may not have been properly distributed as an irrigated area (Portmann et al., 2010).

Our estimates are slightly lower than those provided by the Global Irrigated Map, which identified 21 thousand hectares of irrigated area using remote sensing products. The Global Irrigated Map distributed the irrigated area based on previous knowledge from the GMIA dataset. It was anticipated that the estimates from the Global Irrigated Map would be higher, given its use of higher spatial resolution and recent satellite observations to capture finer details. This resolution allowed us to identify denser irrigation in regions already identified as irrigated in the GMIA dataset, as well as to discover newly irrigated croplands in regions previously not identified as irrigated (Meier et al., 2018). While in some NUTS 2 regions, both our estimates and the Global Irrigated Areas dataset show higher irrigated areas compared to other existing maps, the locations of these irrigated pixels vary between the two maps (Figure 13). Additional irrigated areas were identified in Freiburg, which is located to the west of the French-German border. This could be because irrigation is only used as a supplementary measure on crops during
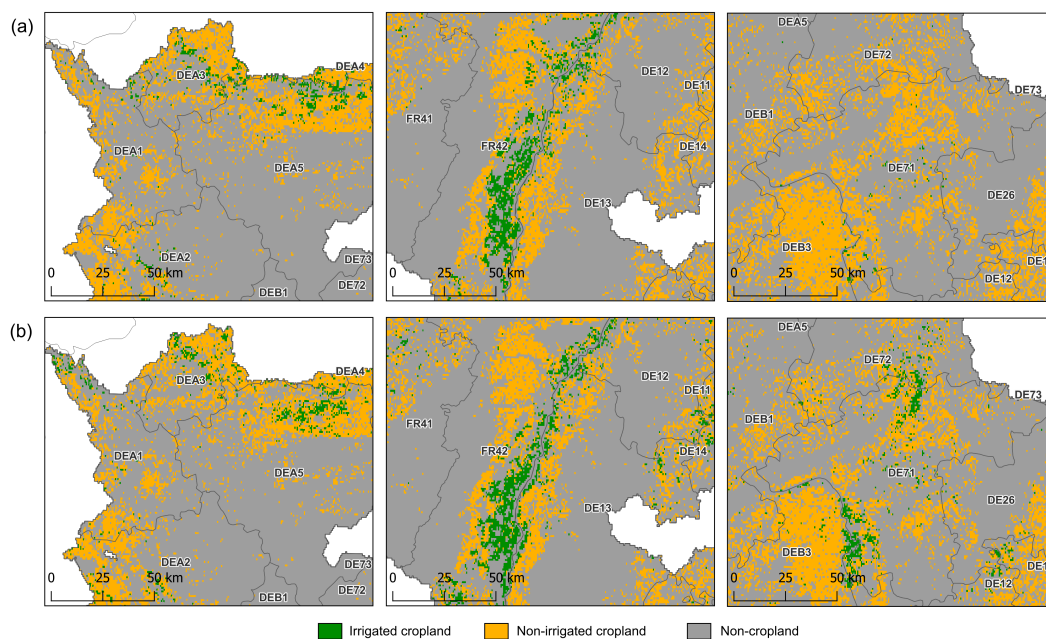
Figure 11. Difference in the extent of irrigated area between **(a)** 2018 and **(b)** 2019.

dry periods. Therefore, it is possible that the irrigated data from the Global Irrigated Area, which represents irrigation from 1999 to 2012, does not accurately represent irrigation dynamics during the study period.

In contrast, our estimates of irrigated areas are lower compared to those provided by the Global Irrigated Areas Map (GIAM), which estimates an exceptionally high value of around 1.4×10^6 hectares. The high value of GIAM estimates can be attributed

380   to overestimation in the eastern part of the basin. However, it underestimates the irrigated areas in the Rhine valley, which is identified as the most heavily irrigated area in the basin in other products. This serves as an example that a different approach, spatial resolutions, and input data to identify the irrigated map can yield different results. Additionally, the reference period of existing products vary, which may not be representative of the period used in this study. The difference in the identified irrigated area was also experienced by Meier et al. (2018) which used GMIA data from 2005 to identify the irrigated area that

385   is representative for the period 1999–2012.

4   Discussion

The results of this study demonstrate the potential of using evapotranspiration estimates from a spatially distributed hydrological model and satellite observations of land surface temperature to detect and monitor irrigated areas. Irrigation modulates the partitioning of surface energy and water balance through evapotranspiration which leads to reductions in land surface tempera-

390   ture in irrigated croplands. These impacts of irrigation on land surface temperature were also used in previous regional studies to identify irrigated areas (Shahriar Pervez et al., 2014; van Dijk et al., 2018). By coupling surface energy with water balance
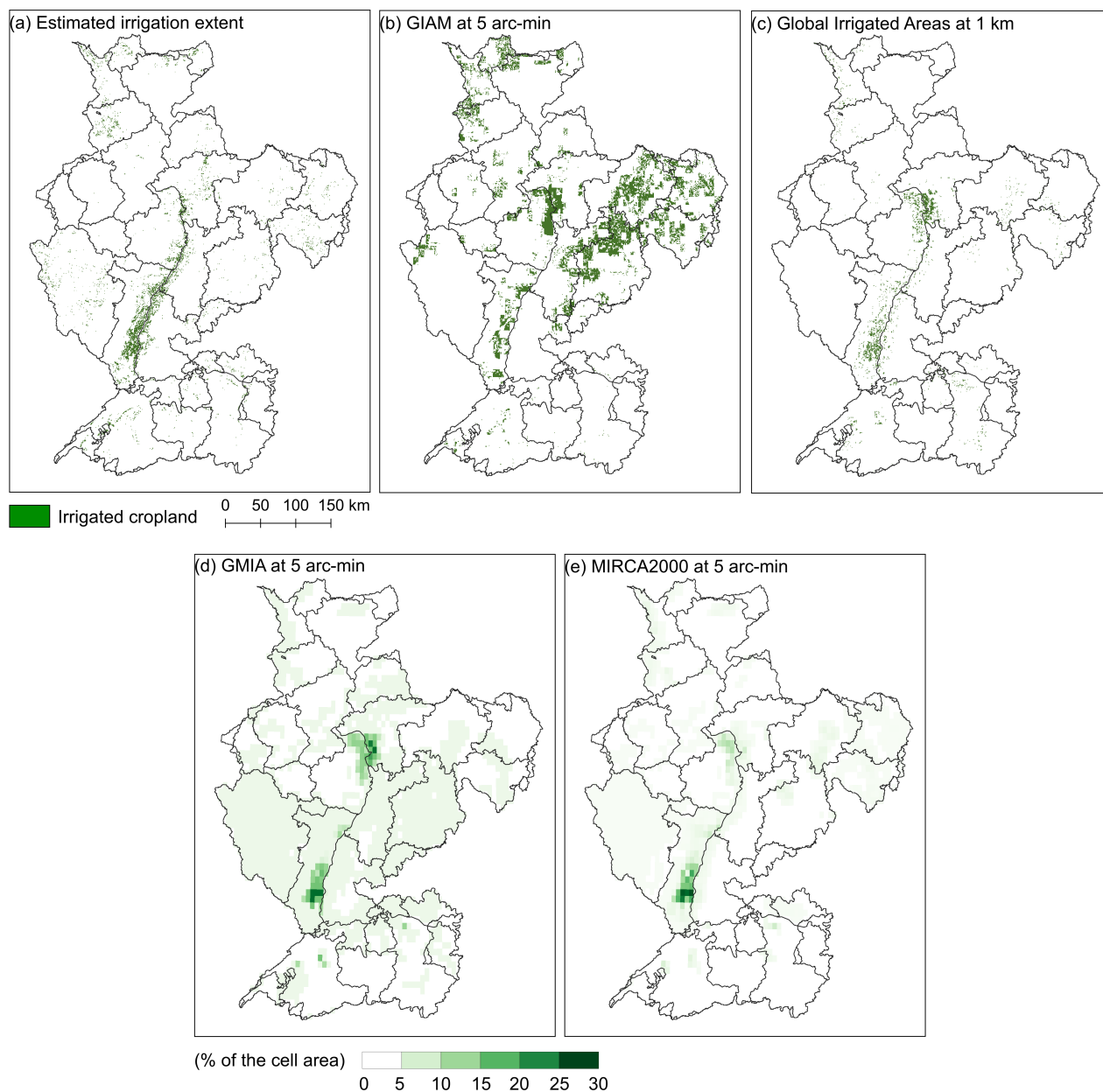
Figure 12. Comparison the estimated irrigation extent using land surface temperature with current irrigation maps.

in the model, we can improve the identification of irrigated areas, particularly in regions where precipitation patterns coincide with irrigation cycles. Although our estimates were produced without relying on existing maps to determine the location of irrigated areas, the proposed methodology can reasonably approximate the extent of irrigated areas when evaluated against

395 existing irrigation maps (Figure 8).
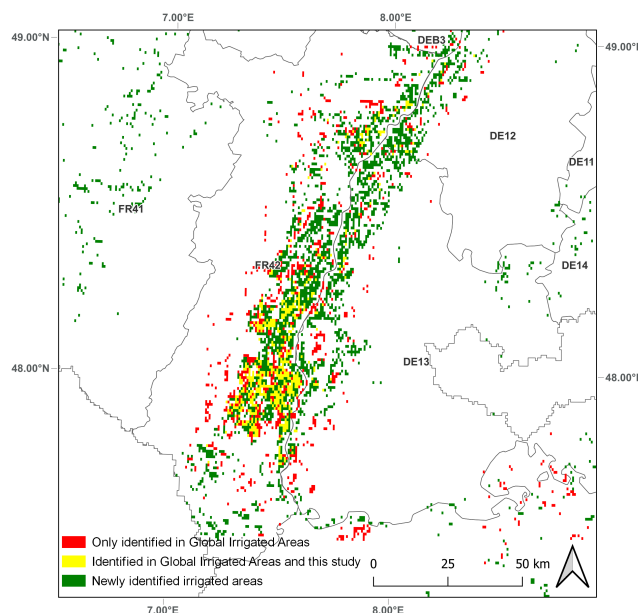
Figure 13. Irrigated areas in the Rhine valley. The green areas are newly identified irrigated area, the yellow area are irrigated areas identified both in this study and in Global Irrigated Area by Meier et al. (2018), and the red areas are irrigated areas which were only identified in Global Irrigated Area.

Nevertheless, potential uncertainties may still arise from the spatial resolution of mapping units in the model, where a 1 km^2 pixel is considered in binary classification. Such disparities between the spatial resolution of mapping units and the actual size of irrigation plots in the field may lead to the identification of additional areas as irrigated lands (Colombo et al., 2008). To resolve fragmented irrigated areas, finer resolution maps are usually used, as they offer fewer mixed signals over regions

400 with heterogeneous land cover types (Velpuri et al., 2009). However, this comes with a trade off in terms of longer data processing times. Although a spatial resolution of 1 km^2 is suitable for water management at the basin level and performed well in the study area, it may not be able to capture irrigated areas in regions with significant small fragmented agricultural holdings and heterogeneous land use (Figure 8). This underscores the necessity of including methodology for irrigated area estimations in regions characterized by fragmented agricultural holdings (i.e., sub-pixel calculations in Global Irrigated Map

405 (GIAM) (Thenkabail et al., 2009) or regional field size factor (Salmon et al., 2015)). Nevertheless, the approach to determine these factors requires validation, as it may introduce uncertainties in the outcome (Meier et al., 2018).

Additional uncertainties are also attributed to the input datasets and methodology. The input datasets of our study consist of evapotranspiration estimates from a hydrological model and satellite observations of land surface temperature. Since satellite observations implicitly capture various types of evapotranspiration, the parameterization (i.e., soil parameters, rooting

410 zone) within the hydrological model to estimate evapotranspiration could yield land surface temperature estimates that do not accurately indicate irrigation. A study by van Dijk et al. (2015) demonstrates that satellite observations captured additional

evapotranspiration from groundwater-dependent ecosystems, which is not attributed to precipitation. This justifies the decision to mask out wetlands and forests to eliminate additional sources of evapotranspiration such as lateral inflow and deep root water intake before applying the algorithm, as these processes can produce a misleading indication of irrigation. Misclassification in
415 CORINE land cover and land use data which were used to mask out noncropland pixels for the classification process introduces further uncertainties. Despite the high accuracy of the land use data, occurrences of false classification were observed (not shown), thereby propagating error to our estimates of irrigated areas. In particular, mixed land use areas where pasture and cropland are difficult to map are likely to have higher error rates due to misclassification. Furthermore, the absence of pixel area fractions in the cropland data sourced from the land use land cover dataset may potentially lead to an overestimation of
420 the irrigation area.

Our analysis indicates that fluctuations in the total irrigated area within the Rhine basin are particularly influenced by precipitation. Decreased precipitation leads to reductions in the extent of irrigated area in the driest year. This trend was also reported in other regional studies (see Afghanistan (Shahriar Pervez et al., 2014); the Ebro basin (Deines et al., 2019)) that show influence of limited water availability on irrigation decision making. A study by Foster et al. (2014) demonstrate that the
425 reduction in irrigated area is influenced by field-level decision-making, where farmers choose to maintain sufficient soil water availability to minimize the risk of significant production losses by increasing water supply to a smaller area. This choice is constrained by regulatory restrictions that limit water abstractions. Although other factors influencing irrigation dynamics, such as improvements in irrigation efficiency, regulations, and restrictions on groundwater, were not studied, they may significantly influence the temporal dynamics of irrigation and needs to be investigated.

430 Although the total irrigated area comprises only about 2% of the total basin, peaks in land surface temperature differences were observed during the summer months (JJA) when precipitation cannot compensate high crop evapotranspiration. This translates to high irrigation rates being applied to offset the high rate of crop evapotranspiration, which puts additional pressure on limited water availability. Under changing climate conditions, projections for the Rhine Basin indicate that a combination of changes in snow melting processes and increased potential evapotranspiration will result in decreased summer discharge
435 (Buitink et al., 2021). This scenario highlights the urgency of addressing irrigation water demands and potential water deficits during summer months. However, these areal expansions and/or reductions throughout the study period were only detected in agricultural land cover since the classification was performed within the agricultural class. Thus, any changes in land use and land cover were not accounted in the results. It should be mentioned that the evaluation was performed with N=10, and a longer time series will likely reduce random error (Thiese et al., 2016).

440 **5 Conclusions**

We used an energy balance approach to identify irrigated areas using land surface temperature derived from the evapotranspiration of a hydrological model and land surface temperature products from MODIS. The proposed methodology was able to identify irrigated areas in the Rhine basin, showing good agreement with sub-national statistics. However, the performance of the model deteriorates when applied to regions with small fragmented agricultural areas due to differences between the spatial

445 resolution of mapping units and the actual size of irrigation plots. When evaluated against existing irrigation products, our results show underestimation and overestimation which can be attributed to spatial resolution, input data, reference period, and processing techniques. Although technically feasible, comparing our estimate of irrigated area with other irrigation maps would not necessarily mean validation, as those maps have typically not undergone comprehensive validation against actual ground observations.

450 The results of our study reveal annual variability in irrigated areas, highlighting the necessity of gathering multiyear data to improve water resources management. These variations are attributed to decreased irrigated area during dry periods, underscoring the profound influence of water availability on irrigation management. While our study does not evaluate other contributing factors besides climatic variables, such as policy measures, previous studies demonstrate the influence of regulatory frameworks on irrigation water use, which need to be studied. For example, our findings reveal a general decrease in

455 the total irrigated area during periods of low precipitation. However, on a regional level, we observe an opposite trend with an increase in irrigated area during dry periods.

Uncertainties and limitations are inherent in our results. Uncertainties could be introduced through the classification process, input data, spatial resolution, and evapotranspiration products from the hydrological model. It should be noted that our approach currently predicts annual irrigated areas due to limitations imposed by the availability of thermal imagery. This constraint

460 complicates the applicability of our method for weekly or even daily observations. Thus, considering the temporal resolution of land surface temperature data becomes important, as enhancing this resolution has the potential to improve the methodology for identifying irrigated areas, particularly in regions where precipitation occasionally aligns with irrigation cycles.

Appendix A: Random forest performance on test data

The performance of random forest model was evaluated using several performance evaluation metrics which are obtained from

465 true negatives (TN), true positives (TP), false negatives (FN), and false positives (FP). The recall measures the portion of irrigated areas in test set which were correctly identified. The precision shows the portion of pixels identified as irrigated which are actually irrigated. The F1 score combines both recall and precision into a unified metric.

$$Accuracy = \frac{\Sigma(TP+TN)}{\Sigma(TP+FP+TN+FN)} \tag{A1}$$

$$Recall = \frac{\Sigma TP}{\Sigma(TP+FN)} \tag{A2}$$

470 $$Precision = \frac{\Sigma TP}{\Sigma(TP+FP)} \tag{A3}$$

$$F1 = \frac{2 \times Recall \times Precision}{Rcall + Precision} \tag{A4}$$

Table A1. The accuracy, precision, recall, and F_1 score of the random forest model on training data used to classify irrigated areas based on land surface temperature differences for the years 2010 to 2019

Year	Accuracy	Precision	Recall	F_1
2010	0.941	0.934	0.945	0.939
2011	0.944	0.940	0.952	0.943
2012	0.960	0.963	0.955	0.958
2013	0.926	0.918	0.933	0.924
2014	0.940	0.941	0.933	0.937
2015	0.966	0.964	0.967	0.966
2016	0.921	0.922	0.921	0.921
2017	0.924	0.919	0.925	0.921
2018	0.986	0.988	0.985	0.986
2019	0.924	0.919	0.925	0.921

Appendix B: Interannual variability of irrigated area
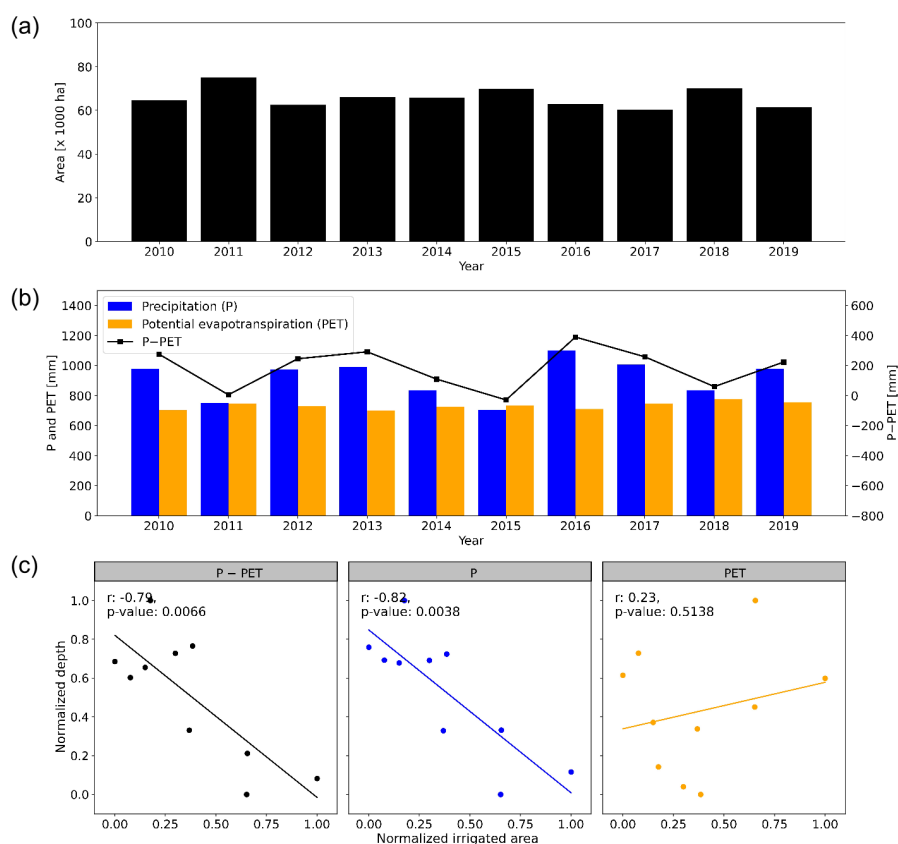
Figure B1. (a) The annual sum of climatic variables: precipitation, evapotranspiration, and the difference for the period from 2010 to 2019 for Alsace (FR42). **(b)** Linear regression analysis is performed for each climatic variable compared to the annual irrigated area.

Code and data availability. Code and data will be published on 4TU repository. The radiation term for input of the land surface temperature module were retrieved from https://datalsasaf.lsasvcs.ipma.pt/PRODUCTS/MSG/MDIDSSF/NETCDF/ and the surface albedo was retrieved

475 from https://datalsasaf.lsasvcs.ipma.pt/PRODUCTS/MSG/MDAL/NETCDF/. The MODIS Land Surface Temperature data from the Terra and Aqua sensor were retrieved from https://lpdaac.usgs.gov/. The irrigation statistics at NUTS level 2 for data validation are available at Eurostat database (https://ec.europa.eu/eurostat/databrowser/view/EF_POIRRIG/default/table?lang=en).

Author contributions. DP was responsible for developing the methodologies, performing the analysis, and writing the article. AJT and AHW improved the article, reviewed the figures, and refined the experimental setup. AJT and AHW supervise DP in their PhD program.

480 *Competing interests.* Two of the (co)-authors are members of the editorial board of Hydrology and Earth System Sciences and the contact author has declared none other competing interests.

Acknowledgements. This research was funded through by the EU Commission under the Horizon Europe 2020 STARS4WATER project (www.stars4water.eu), Grant agreement ID 101059372 (https://cordis.europa.eu/project/id/101059372). We would like to thank Joost Buitink for providing forcing data and model setup for wflow_sbm.

References

Allen, R. G., Pereira, L. S., Raes, D., Smith, M., et al.: Crop evapotranspiration-Guidelines for computing crop water requirements-FAO Irrigation and drainage paper 56, Fao, Rome, 300, D05 109, 1998.

Ambika, A. K., Wardlow, B., and Mishra, V.: Remotely sensed high resolution irrigated area mapping in India for 2000 to 2015, Scientific data, 3, 1–14, 2016.

Berbel, J., Borrego-Marin, M. M., Exposito, A., Giannoccaro, G., Montilla-Lopez, N. M., and Roseta-Palma, C.: Analysis of irrigation water tariffs and taxes in Europe, Water Policy, 21, 806–825, 2019.

BfG: Das Niedrigwasser 2018, Online, available at: https://doi.bafg.de/BfG/2019/Niedrigwasser_2018.pdf, 2019.

Boretti, A. and Rosa, L.: Reassessing the projections of the world water development report, NPJ Clean Water, 2, 15, 2019.

Breiman, L.: Random forests, Machine learning, 45, 5–32, 2001.

Buitink, J., Melsen, L. A., and Teuling, A. J.: Seasonal discharge response to temperature-driven changes in evaporation and snow processes in the Rhine Basin, Earth System Dynamics, 12, 387–400, https://doi.org/10.5194/esd-12-387-2021, 2021.

Buitink, J., Tsiokanos, A., Geertsma, J., ten Velden, C., Bouaziz, L., and Weiland, F.: Implications of the KNMI'23 climate scenarios for the discharge of the Rhine and Meuse, https://publications.deltares.nl/11209265_002_0003.pdf, 2023.

Colombo, R., Meroni, M., Marchesi, A., Busetto, L., Rossini, M., Giardino, C., and Panigada, C.: Estimation of leaf and canopy water content in poplar plantations by means of hyperspectral indices and inverse modeling, Remote sensing of environment, 112, 1820–1834, 2008.

Dari, J., Quintana-Seguí, P., Escorihuela, M. J., Stefan, V., Brocca, L., and Morbidelli, R.: Detecting and mapping irrigated areas in a Mediterranean environment by using remote sensing soil moisture and a land surface model, Journal of Hydrology, 596, 126 129, 2021.

Deines, J. M., Kendall, A. D., Crowley, M. A., Rapp, J., Cardille, J. A., and Hyndman, D. W.: Mapping three decades of annual irrigation across the US High Plains Aquifer using Landsat and Google Earth Engine, Remote Sensing of Environment, 233, 111 400, 2019.

Döll, P. and Siebert, S.: Global modeling of irrigation water requirements, Water resources research, 38, 8–1, 2002.

Droogers, P., Immerzeel, W., and Lorite, I.: Estimating actual irrigation application by remotely sensed evapotranspiration observations, Agricultural Water Management, 97, 1351–1359, 2010.

Eilander, D., van Verseveld, W., Yamazaki, D., Weerts, A., Winsemius, H. C., and Ward, P. J.: A hydrography upscaling method for scale-invariant parametrization of distributed hydrological models, Hydrology and Earth System Sciences, 25, 5287–5313, https://doi.org/10.5194/hess-25-5287-2021, 2021.

European Environment Agency: Corine Land Cover (CLC) 2018, Version 20, Retrieved from https://land.copernicus.eu/pan-european/corine-land-cover/clc2018?tab=metadatA, 2018.

Eurostat: National Reference Metadata in ESS Standard for Quality Reports Structure (ESQRS), https://ec.europa.eu/eurostat/cache/metadata/EN/ef_esqrs_de.htm, Retrieved May 3, 2024, 2016.

Fader, M., Shi, S., von Bloh, W., Bondeau, A., and Cramer, W.: Mediterranean irrigation under climate change: more efficient irrigation needed to compensate for increases in irrigation water requirements, Hydrology and Earth System Sciences, 20, 953–973, https://doi.org/10.5194/hess-20-953-2016, 2016.

Farr, T. G., Rosen, P. A., Caro, E., Crippen, R., Duren, R., Hensley, S., Kobrick, M., Paller, M., Rodriguez, E., Roth, L., Seal, D., Shaffer, S., Shimada, J., Umland, J., Werner, M., Oskin, M., Burbank, D., and Alsdorf, D. E.: The Shuttle Radar Topography Mission, Reviews of Geophysics, 45, RG2004, https://doi.org/10.1029/2005RG000183, 2007.

Feddes, R. A., Kowalik, P., Kolinska-Malinka, K., and Zaradny, H.: Simulation of field water uptake by plants using a soil water dependent root extraction function, Journal of Hydrology, 31, 13–26, https://doi.org/https://doi.org/10.1016/0022-1694(76)90017-2, 1976.

Fischer, G., Tubiello, F. N., Van Velthuizen, H., and Wiberg, D. A.: Climate change impacts on irrigation water requirements: Effects of mitigation, 1990–2080, Technological Forecasting and Social Change, 74, 1083–1107, 2007.

525 Foster, T., Brozović, N., and Butler, A. P.: Modeling irrigation behavior in groundwater systems, Water resources research, 50, 6370–6389, 2014.

Hanel, M., Rakovec, O., Markonis, Y., Máca, P., Samaniego, L., Kyselỳ, J., and Kumar, R.: Revisiting the recent European droughts from a long-term perspective, Scientific reports, 8, 1–11, 2018.

Iglesias, A., Garrote, L., Quiroga, S., and Moneo, M.: A regional comparison of the effects of climate change on agricultural crops in Europe,
530 Climatic change, 112, 29–46, 2012.

Imhoff, R., Van Verseveld, W., Van Osnabrugge, B., and Weerts, A.: Scaling point-scale (pedo) transfer functions to seamless large-domain parameter estimates for high-resolution distributed hydrologic modeling: An example for the Rhine River, Water Resources Research, 56, e2019WR026 807, 2020.

Jacquette, E., Al Bitar, A., Mialon, A., Kerr, Y., Quesney, A., Cabot, F., and Richaume, P.: SMOS CATDS level 3 global products over land,
535 in: Remote Sensing for Agriculture, Ecosystems, and Hydrology XII, vol. 7824, pp. 137–142, SPIE, 2010.

Jalilvand, E., Tajrishy, M., Hashemi, S. A. G. Z., and Brocca, L.: Quantification of irrigation water using remote sensing of soil moisture in a semi-arid region, Remote Sensing of Environment, 231, 111 226, 2019.

Konapala, G., Mishra, A. K., Wada, Y., and Mann, M. E.: Climate change will affect global water availability through compounding changes in seasonal precipitation and evaporation, Nature communications, 11, 3044, 2020.

540 Laaha, G., Gauster, T., Tallaksen, L. M., Vidal, J.-P., Stahl, K., Prudhomme, C., Heudorfer, B., Vlnas, R., Ionita, M., Van Lanen, H. A. J., Adler, M.-J., Caillouet, L., Delus, C., Fendekova, M., Gailliez, S., Hannaford, J., Kingston, D., Van Loon, A. F., Mediero, L., Osuch, M., Romanowicz, R., Sauquet, E., Stagge, J. H., and Wong, W. K.: The European 2015 drought from a hydrological perspective, Hydrology and Earth System Sciences, 21, 3001–3024, https://doi.org/10.5194/hess-21-3001-2017, 2017.

Lehner, B., Verdin, K., and Jarvis, A.: New global hydrography derived from spaceborne elevation data, Eos, Transactions American Geo-
545 physical Union, 89, 93–94, 2008.

Liu, Y., Dorigo, W., Parinussa, R., de Jeu, R., Wagner, W., McCabe, M., Evans, J., and van Dijk, A.: Trend-preserving blending of passive and active microwave soil moisture retrievals, Remote Sensing of Environment, 123, 280–297, https://doi.org/https://doi.org/10.1016/j.rse.2012.03.014, 2012.

Martens, B., Miralles, D. G., Lievens, H., van der Schalie, R., de Jeu, R. A. M., Fernández-Prieto, D., Beck, H. E., Dorigo, W. A., and
550 Verhoest, N. E. C.: GLEAM v3: satellite-based land evaporation and
root-zone soil moisture, Geoscientific Model Development, 10, 1903–1925, https://doi.org/10.5194/gmd-10-1903-2017, 2017.

Meier, J., Zabel, F., and Mauser, W.: A global approach to estimate irrigated areas – a comparison between different data and statistics, Hydrology and Earth System Sciences, 22, 1119–1133, https://doi.org/10.5194/hess-22-1119-2018, 2018.

Monfreda, C., Ramankutty, N., and Foley, J. A.: Farming the planet: 2. Geographic distribution of crop areas, yields, physiological types,
555 and net primary production in the year 2000, Global biogeochemical cycles, 22, 2008.

Ozdogan, M. and Gutman, G.: A new methodology to map irrigated areas using multi-temporal MODIS and ancillary data: An application example in the continental US, Remote Sensing of Environment, 112, 3520–3537, 2008.

Peña-Arancibia, J. L., Mainuddin, M., Kirby, J. M., Chiew, F. H., McVicar, T. R., and Vaze, J.: Assessing irrigated agriculture's surface water and groundwater consumption by combining satellite remote sensing and hydrologic modelling, Science of the Total Environment, 542, 372–382, 2016.

Portmann, F. T., Siebert, S., and Döll, P.: MIRCA2000—Global monthly irrigated and rainfed crop areas around the year 2000: A new high-resolution data set for agricultural and hydrological modeling, Global biogeochemical cycles, 24, 2010.

Rauthe, M., Steiner, H., Riediger, U., Mazurkiewicz, A., Gratzki, A., et al.: A Central European precipitation climatology–Part I: Generation and validation of a high-resolution gridded daily data set (HYRAS), Meteorologische Zeitschrift, 22, 235–256, 2013.

Salmon, J., Friedl, M. A., Frolking, S., Wisser, D., and Douglas, E. M.: Global rain-fed, irrigated, and paddy croplands: A new high resolution map derived from remote sensing, crop inventories and climate data, International Journal of Applied Earth Observation and Geoinformation, 38, 321–334, https://doi.org/https://doi.org/10.1016/j.jag.2015.01.014, 2015.

Shahriar Pervez, M., Budde, M., and Rowland, J.: Mapping irrigated areas in Afghanistan over the past decade using MODIS NDVI, Remote Sensing of Environment, 149, 155–165, https://doi.org/https://doi.org/10.1016/j.rse.2014.04.008, 2014.

Siebert, S., Döll, P., Hoogeveen, J., Faures, J.-M., Frenken, K., and Feick, S.: Development and validation of the global map of irrigation areas, Hydrology and Earth System Sciences, 9, 535–547, 2005.

Siebert, S., Henrich, V., Frenken, K., and Burke, J.: Update Of The Digital Global Map Of Irrigation Areas to Version 5, Tech. rep., Rheinische Friedrich-Wilhelms-University, Bonn, Germany/Food and Agriculture Organization of the United Nations, Rome, Italy, 2013.

Spinoni, J., Vogt, J. V., Naumann, G., Barbosa, P., and Dosio, A.: Will drought events become more frequent and severe in Europe?, International Journal of Climatology, 38, 1718–1736, 2018.

Talsma, C. J., Good, S. P., Jimenez, C., Martens, B., Fisher, J. B., Miralles, D. G., McCabe, M. F., and Purdy, A. J.: Partitioning of evapotranspiration in remote sensing-based models, Agricultural and Forest Meteorology, 260-261, 131–143, https://doi.org/https://doi.org/10.1016/j.agrformet.2018.05.010, 2018.

Thenkabail, P. S., Biradar, C. M., Noojipady, P., Dheeravath, V., Li, Y., Velpuri, M., Gumma, M., Gangalakunta, O. R. P., Turral, H., Cai, X., et al.: Global irrigated area map (GIAM), derived from remote sensing, for the end of the last millennium, International journal of remote sensing, 30, 3679–3733, 2009.

Thiese, M. S., Ronna, B., and Ott, U.: P value interpretations and considerations, Journal of thoracic disease, 8, E928, 2016.

Thom, A. S.: Momentum, mass and heat exchange of plant communities, Vegetation and the Atmosphere, 4, 57–109, 1975.

Toreti, A., Belward, A., Perez-Dominguez, I., Naumann, G., Luterbacher, J., Cronie, O., Seguini, L., Manfron, G., Lopez-Lozano, R., Baruth, B., van den Berg, M., Dentener, F., Ceglar, A., Chatzopoulos, T., and Zampieri, M.: The Exceptional 2018 European Water Seesaw Calls for Action on Adaptation, Earth's Future, 7, 652–663, https://doi.org/https://doi.org/10.1029/2019EF001170, 2019.

Trigo, I. F., Dacamara, C. C., Viterbo, P., Roujean, J.-L., Olesen, F., Barroso, C., de Coca, F. C., Carrer, D., Freitas, S. C., García-Haro, J., Geiger, B., Gellens-Meulenberghs, F., Ghilain, N., Meliá, J., Pessanha, L., Siljamo, N., and Arboleda, A.: The Satellite Application Facility for Land Surface Analysis, International Journal of Remote Sensing, 32, 2725–2744, https://doi.org/10.1080/01431161003743199, 2011.

van Dijk, A., Warren, G., Van Niel, T., Byrne, G., Pollock, D., and Doody, T.: Derivation of data layers from medium resolution remote sensing to support mapping of groundwater dependent ecosystems, https://doi.org/10.13140/RG.2.1.1260.6804, 2015.

van Dijk, A. I. J. M., Schellekens, J., Yebra, M., Beck, H. E., Renzullo, L. J., Weerts, A., and Donchyts, G.: Global 5 km resolution estimates of secondary evaporation including irrigation through satellite data assimilation, Hydrology and Earth System Sciences, 22, 4959–4980, https://doi.org/10.5194/hess-22-4959-2018, 2018.

595   Van Osnabrugge, B., Uijlenhoet, R., and Weerts, A.: Contribution of potential evaporation forecasts to 10-day streamflow forecast skill for
       the Rhine River, Hydrology and Earth System Sciences, 23, 1453–1467, 2019.

       van Verseveld, W. J., Weerts, A. H., Visser, M., Buitink, J., Imhoff, R. O., Boisgontier, H., Bouaziz, L., Eilander, D., Hegnauer, M., ten Velden,
       C., and Russell, B.: Wflow_sbm v0.7.3, a spatially distributed hydrological model: from global data to local applications, Geoscientific
       Model Development, 17, 3199–3234, https://doi.org/10.5194/gmd-17-3199-2024, 2024.

600   Velpuri, N., Thenkabail, P. S., Gumma, M. K., Biradar, C., Dheeravath, V., Noojipady, P., and Yuanjie, L.: Influence of resolution in irrigated
       area mapping and area estimation, Photogrammetric Engineering & Remote Sensing, 75, 1383–1395, 2009.

       Vertessy, R. A. and Elsenbeer, H.: Distributed modeling of storm flow generation in an Amazonian rain forest catchment: Effects of model
       parameterization, Water Resources Research, 35, 2173–2187, 1999.

       Wagner, W., Dorigo, W., de Jeu, R., Fernandez, D., Benveniste, J., Haas, E., and Ertl, M.: Fusion of active and passive microwave observations
605   to create an essential climate variable data record on soil moisture, ISPRS Annals of the Photogrammetry, Remote Sensing and Spatial
       Information Sciences, I-7, 315–321, https://doi.org/10.5194/isprsannals-I-7-315-2012, 2012.

       Wan, Z., Hook, S., and Hulley, G.: MODIS/Aqua Land Surface Temperature/Emissivity Daily L3 Global 1km SIN Grid V061, Data set,
       accessed 2024-05-08 from https://doi.org/10.5067/MODIS/MYD11A1.061, 2021a.

       Wan, Z., Hook, S., and Hulley, G.: MODIS/Terra Land Surface Temperature/Emissivity Daily L3 Global 1km SIN Grid V061, Data set,
610   accessed 2024-05-08 from https://doi.org/10.5067/MODIS/MOD11A1.061, 2021b.

       Wang, K. and Dickinson, R. E.: A review of global terrestrial evapotranspiration: Observation, modeling, climatology, and climatic variability,
       Reviews of Geophysics, 50, 2012.

       Zink, M., Mai, J., Cuntz, M., and Samaniego, L.: Conditioning a Hydrologic Model Using Patterns of Remotely Sensed Land Surface
       Temperature, Water Resources Research, 54, 2976–2998, https://doi.org/https://doi.org/10.1002/2017WR021346, 2018.